HIGH PERFORMANCE FLOWER SHAPE MANGANESE OXIDE FOR ASYMMETRIC SUPERCAPACITOR DEVICE

I. I. Misnon[1], B. Vidyadharan[2], R. A. Aziz[3], R. Jose[4*]

[1,2,3,4]Nanostructured Renewable Energy Material Laboratory, Faculty of Industrial Sciences & Technology, Universiti Malaysia Pahang, Lebuhraya Tun Razak, 26300 Gambang, Kuantan, Pahang

ABSTRACT

A flower shaped manganese oxide have been synthesized using simple and low temperature procedure. Subsequently, an asymmetric supercapacitor is fabricated using manganese oxide and activated carbon as positive and negative electrode in aqueous electrolyte. The supercapacitor was measured at open windows 2.0 V showing energy density of 25.79 Wh/kg at power density of 100 W/kg. The supercapacitor stability was tested at 3 A/g and showing specific capacitance retention of 95% after 850 cycles.

KEYWORDS: *Energy storage; supercapacitor; manganese oxide; asymmetric capacitor.*

1.0 INTRODUCTION

Supercapacitor is an energy storage devices that provide advantages compared to conventional capacitor including high specific capacitance (C_S) and energy density (E_D) (Conway, 1999). The energy stored in supercapacitor are governed by two mechanisms, (i) electrical double layer capacitor (EDLC)–ions adsorption on the electrode-electrolyte interface and fast and (ii) pseudocapacitance (PC)–a fast and reversible redox reaction mechanism (Simon & Gogotsi, 2008). Asymmetric supercapacitor (ASC) is usually fabricated by combining PC material (eg: metal oxides) as positive electrode and EDLC material (eg: activated carbon, AC) as negative electrode, separated by permeable separator in electrolyte environment. This combination is essential to obtained maximum working potential (1.8–2.4 V).

The current research focused on metal oxides and composites development to enhance E_D and power density (P_D) as this type of material is having higher theoretical capacitance values exceeding 1000 F/g (Liang et al., 2012; Toupin et al., 2002; Vidyadharan et al., 2014; Zhang et al., 2012).

The supercapacitors fabricated using the hydrated ruthenium oxide ($RuO_2.nH_2O$) electrodes are currently the record holder in terms of specific capacitance (C_S ~ 720 F/g in case of hydrothermal synthesis). This contributes by several factors including high conductivity and crystallite water molecules enhance the electrons and ions hopping.

* Corresponding Email: rjose@ump.edu.my

However, RuO_2 are relatively rare abundance makes them expensive thereby offering barriers for mass production (Yan et al., 2014; Zheng et al., 1995). Several metal oxide has been studied to overcome this drawback, among them is manganese oxide (MnO_2). Birnessite-type MnO_2 (δ-MnO_2) gained much attention as an electrode for supercapacitors because of its thin sheet-like layered structure stabilized by an alkali ion (eg: K^+ or Na^+) and crystallized water is similar to that of the $RuO_2.nH_2O$ (Dmowski et al., 2002; Kim & Kim, 2006).

In this article, δ-MnO_2 is prepared through a simple and low temperature synthesis condition. The ASC was prepared in coin cell type assembly using aqueous potassium sulfate (K_2SO_4) electrolyte. This is in order to enhance the potential window of ASC and enhance E_D. The MnO_2//AC ASC shows a promising potential window of 2.0 V and demonstrated E_D of 25.79 Wh/kg at P_D 100 W/kg.

2.0 EXPERIMENTAL

2.1 Material Synthesis

The synthesis of MnO_2 was carried out using hydrothermal method. In a typical experiment 4.5 mmol of potassium permanganate ($KMnO_4$, BDH Chemicals) solution was mixed with 1.5 mmol ammonium persulfate ($(NH_4)_2S_2O_8$, Aldrich) in a Teflon lined stainless steel reactor. After being stirred for 20 min, the reactor was kept in an oven at 90 ^oC for 24 h. After cooling down to room temperature, the brownish precipitate product was filtered; wash thoroughly with DI water until the pH~7, dry at 50^oC for 24 h.

2.2 Material Characterizations

The MnO_2 were characterized by X-ray diffraction (XRD), field emission scanning electron microscope (FESEM), and transmission electron microscopy (TEM). The XRD patterns were acquired on Miniflex II (Rigaku, Japan) X-ray diffractometer employing CuK_α radiation (λ = 1.5406 Å) and Ni- filter. Surface morphology of the samples were investigated using a JSM-7800F (JEOL, Japan) FESEM. The crystal structural details were obtained using Tecnai 20 (FEI, USA) operating at 200 kV accelerated voltage.

2.3 Electrode Fabrication and Supercapacitor Assembly

The positive electrode were prepared by mixing active material, MnO_2 (70 wt%.) with carbon (Super P, 15 wt.%) and polyvinylidene fluoride (PVDF) binder (15 wt%) using N-methyl pyrrolidone (NMP) as a solvent. The above mixture was stirred for 24 h and the slurry obtained thereby was coated onto a pre-cleaned nickel foam (pores per inch; 110 ppi) substrate. The coated electrode was annealed at 60°C oven 24 h and finally pressed at 5 MPa using hydraulic press.

The negative electrode were prepared following the similar procedure with positive electrode by replacing commercial activated carbon (S_{BET}: 1820 m^2/g, Zhejiang Forest

Energy Technology Co. Ltd, China) as the active material. Supercapacitor was assemble in coin cell type case (CR2032) using fibrous glassy carbon as separator and using 0.5M K_2SO_4 electrolyte.

2.4 Electrochemical Analyses

The electrochemical analysis of cyclic voltammetry (CV), Galvanostatic charge-discharge (CDC) and electrochemical impedance spectroscopy (EIS) were acquired using potentiostat (Autolab PGSTAT 30, Eco Chemie B.V., The Netherland) employing NOVA 1.9 software. A platinum rod and Ag/AgCl electrode were used as counter and reference electrode for three-electrode configuration analysis. The supercapacitor cycle stability were measured using battery tester (Neware, China). The specific capacitance (C_S, F/g), energy density (E_D, Wh/kg), power density (P_D, W/kg), internal resistance (I_R, Ω) and coulombic efficiency (η, %) were calculated according to the following Equation (1)–(6):

$$C_S(CV) = \frac{1}{mv(\Delta V)} \int_{Va}^{V_b} i(V)dV \tag{1}$$

$$C_S(CV) = 4\frac{it}{m\Delta V} \tag{2}$$

$$E_D = \frac{1}{2} C_S(\Delta V)^2 \tag{3}$$

$$P_D = \frac{E_D}{t_d} \tag{4}$$

$$I_R = \frac{V_{IR}}{2i} \tag{5}$$

$$\eta = \frac{t_d}{t_c} x100 \tag{6}$$

where m (g) is active mass, v (mV/s) is scan rate, ΔV (V) is the applied potential window (i.e. V_a to V_b), i (A) is current, t_d (s) and t_c (s) are the discharging time and charging time and V_{IR} (V) is the internal resistance potential drop.

3.0 RESULTS AND DISCUSSION

3.1 Physicochemical Properties of MnO_2

The XRD pattern of hydrothermal reaction product of MnO_2 is shown in Figure 1a. The XRD pattern is indexed to the monoclinic potassium birnessite (JCPDF No 43-1456) structure with *C2/m* space group (No. 12) (Ghodbane et al., 2009). The (001) and the (002) planes are typical of the layered structure of δ–MnO_2 whereas the broadened (100) plane indicate crystallized water and formation of water-MnO_2 interlayer (Truong et al., 2012). The basal plane spacing calculated from the (001) plane is ~0.73 nm,

which is the characteristic of the birnessite MnO_2 due to water molecule and intercalated potassium ion.

The FESEM images of MnO_2 at low magnification (Figure 1b) shows uniform flower-like morphology of MnO_2. Using Image-J software measurement, the average diameter of the flowers was ~1.23 µm. A higher magnification FESEM image in Figure 1c clearly shows that the curly and folded thin nanosheets of thickness ~20 nm are branched out from one central zone.

The bright field TEM image of the MnO_2 is shown in Figure 1d. The image indicates that the particles have a coronal spherical morphology, which in turn composed of multilayer hierarchical nanosheets. These curly nanosheets in the sphere are grown from a core during hydrothermal reaction. A high resolution TEM (HRTEM) image of a nanosheet is in Figure 1e. The measured spacing along the (001) plane is ~ 0.65 nm in HRTEM, which is lower than that observed in the XRD pattern (~0.73 nm). This lowering is due to the evaporation of interlayer water molecules under the high energy electron beam irradiation (Liu et al., 2011).

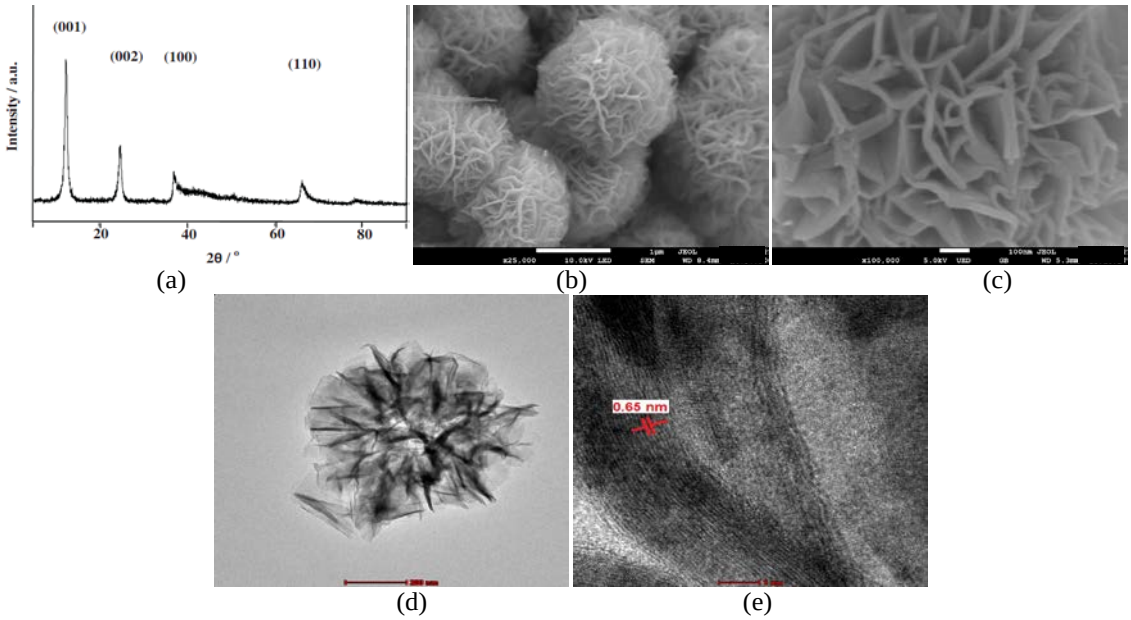

Figure 1. (a) XRD pattern of MnO_2; FESEM micrograph of flower shaped MnO_2 at (b) low and (c) high magnification; (d) TEM and (e) HRTEM image of MnO_2

3.2 Determination of MnO_2//AC Mass Ratio

To balance the charge (q) and maximize C_S, the mass ratio of positive and negative electrode need to be measured. The individual CV scan of MnO_2 and AC is shown in Figure 2a. The MnO_2 electrode potential window is in range 0.0 to 0.9 V whereas for AC is in range -1.1 to 0.0 V, in order to archive supercapacitor working potential of 2.0 V. The CV was measured at scan rate 10 mV/s. The mass ratio of MnO_2 to AC electrode is 0.89, calculated according to Equation (7).

$$\frac{m_+}{m_-} = \frac{C_{S-} \times \Delta V_-}{C_{S+} \times \Delta V_+} \tag{7}$$

3.3 Supercapacitor Performance Analysis

The MnO_2//AC asymmetric supercapacitor CV curve at scan rate 10 mV/s is shown in Figure 2b. It shows that near rectangular CV shape in 2.0 V potential range. The calculated C_S at this scan rate is 54 F/g. To understand the maximum open potential of MnO_2//AC capability, the CDC at 1 A/g was measure in potential range 1.2 to 2.4 V. The CDC curve for CDC at different potential is shown in Figure 2c. The curve shows symmetric triangle of charge and discharge; indicate that the optimum reversibility during charging and discharging. The relation of η, C_S and I_R is shown in Figure 2d. The η is showing decrease trend respect to increased open potential where the efficiency drops from 99.3% at 1.2 V to 89.5% at 2.4 V. The C_S and I_R, however, increase respect to increasing open potential. The C_S is increased from 93 to 137 F/g and the I_R increased from 4.98 to 6.90 Ω. The optimize supercapacitor should having higher η and C_S but minimum I_R. Thus, open potential of 2.0 V is the most promising for MnO_2//AC system.

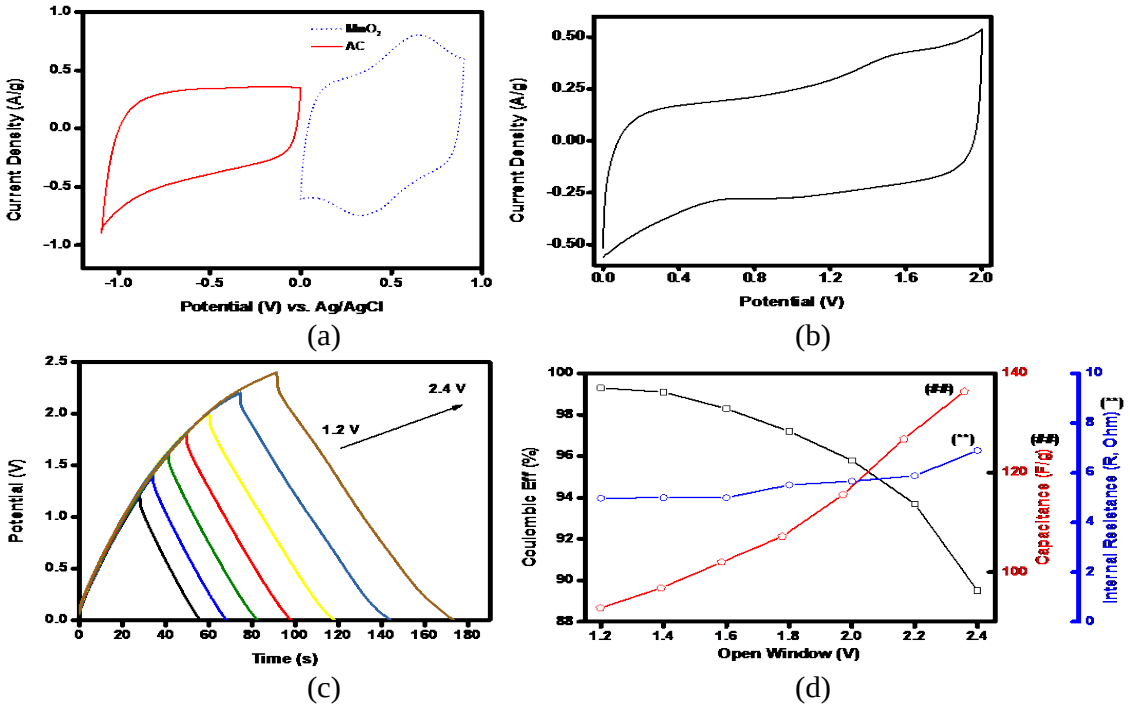

Figure 2. (a) CV curve for MnO_2 and AC electrode; (b) CV curve for MnO_2//AC supercapacitor at 10 mV/s; (c) CDC curve at current density of 1 A/g for potential range 1.2 – 2.4 V; (d) Variation of η, C_S and I_R for different potential

Then, the performance of MnO_2//AC was tested at different current densities ranging from 3 to 0.1 A/g and the CDC curve is shown in Figure 3a. Near triangle shape for each CDC test indicate that high reversibility of the supercapacitor for each current

density. Clearly, as the current desnsity decreases, the discharge time was also increased. This phenomenon related to the higher fraction of active surfaces that contribute to the intercalation – deintercalation of electrolyte ions at lower current density. The ions have slower time to intercate and accumulate on the active site, hence increased the C_S.

The relation of η, C_S and I_R for CDC analysis at different current density was shown in Figure 3b. Similar to analysis in Figure 2d, the η is showing decrease trend respect to decrease current densities where the efficiency is 95.2% at 3 A/g, increased to 97.4% (1 A/g) and decrease to 86.1% at 0.1 A/g. The C_S is dramatically increased from 96 F/g at 3 A/g to 186 F/g at 0.1 A/g. The same trend observed to the I_R where constant increase from 3.33 to 5.95 Ω. In this current density range, the E_D are 13.33, 16.39, 18.28, 19.83 and 25.79 Wh/kg at P_D of 3000, 1000, 500, 300 and 100 W/kg for current density of 3, 1, 0.5, 0.3 and 0.1 A/g, respectively. The Ragone Plot of E_D versus P_D is shown in Figure 3c. The MnO_2//AC supercapacitor was tested for cell stability test for 850 cycles and the evidence was shown in Figure 3d. the device show promising electrochemical stability with the C_S retention ~ 95% after the end of cycle. The η is unchanged at the end of the stability cycle and shows ~94% throughout the test.

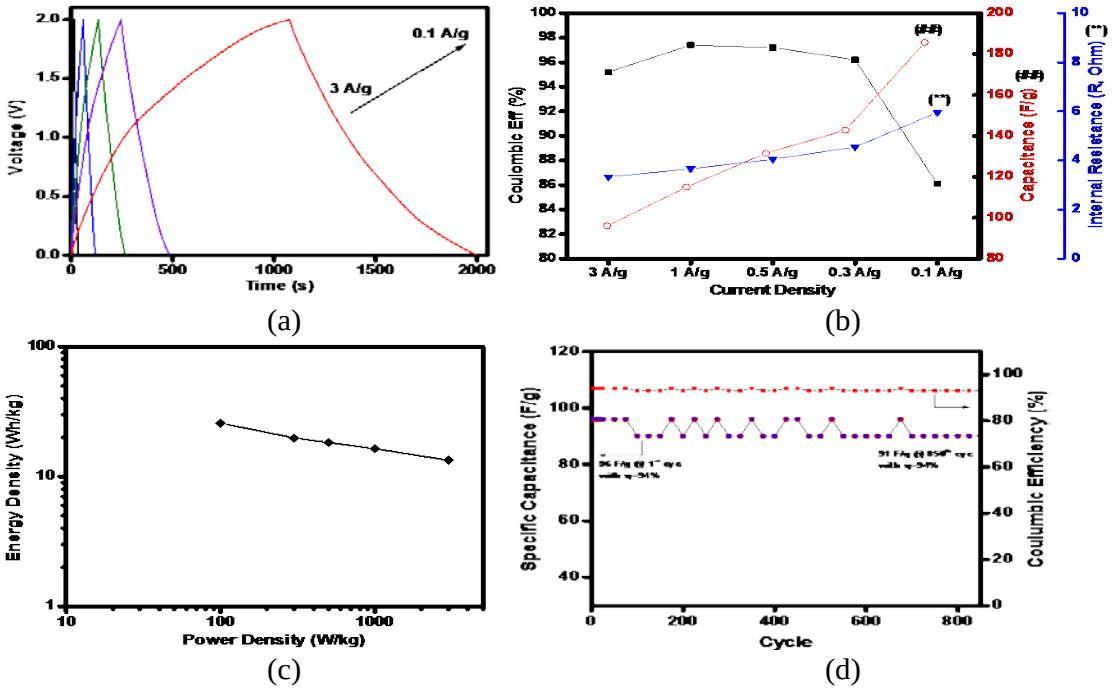

Figure 3. (a) CDC curve at current densities range from 3 – 0.1 A/g; (b) Variation of η, C_S and I_R for different current densities; (c) Ragone plot of MnO_2//AC supercapacitor; (d) Cycle stability test of MnO_2//AC supercapacitor

Table 1 summarizes recent published MnO_2 and AC based ASC. The ASC fabricated in this study shows comparable performance and in most cases it is superior than previous reported work. Finally, the Nyquist plot from EIS measurement of the MnO_2//AC supercapacitor device is shown in Figure 4. The EIS recorded in the frequency range 10

kHz – 10 mHz at a bias voltage of 0.1 V. The EIS spectrum of supercapacitors is routinely deconvoluted into three sections corresponding to three processes offering (i) series resistance (R_S); (ii) Warburg ion diffusion; and (iii) capacitive behavior.

Table 1. Comparison of MnO_2 based ASC device

Electrode		**Electrolyte**	C_S **(F/g) @ rate**	P_D **(kW/kg)**	E_D **(Wh/kg)**	**Ref.**
Positive	**Negative**					
MnO_2	AC	0.1M K_2SO_4	31 (0.55 A/g)	0.605	17.3	(Cottineau et al., 2005)
(Y-α-) MnO_2	AC	1M LiOH	62.4 (100 mA/g)		19.5	(Yuan et al., 2006)
α-MnO_2	AC	0.1M K_2SO_4	21 (2.5 mA/cm^2)	-	11.7	(Brousse et al., 2007)
MnO2 nanorod	AC	0.5M K_2SO_4	53.7 (2C)	2	17	(Qu et al., 2009)
α-MnO_2	AC	0.5M Na_2SO_4	23.1 (12.74 mA/cm^2)	14.7 (P_{max})	10.4	(Wang et al., 2011)
MnO_2 NF	Graphene	0.5M Na_2SO_4	41.7 (1 A/g)	1 (1 A/g)	23.2 (1 A/g)	(Gao et al., 2012)
δ-MnO_2	AC	1M Na_2SO_4	-	0.4 4.0	20.9 8.0	(Zhu et al., 2013)
MnO_2	AC	2M $MgCl_2$	45 (10 mV/s)	1.0	20	(Tomko et al., 2011)
α-MnO_2/ CNT	AC	2M KNO_3	35 (2 mV/s)	123 (P_{max})	21	(Khomenko et al., 2006)
δ-MnO_2	AC	0.5 M K_2SO_4	32.9 (1A/g) 54 (10mV/s)	0.3 24(P_{max})	19.8 25.79	This work

The R_S, determined from the high frequency off-set in the real part of complex impedance of the EIS spectrum are contributed by three main factors viz. (i) electrolyte resistance, (ii) electrode resistance and (iii) electrode–electrolyte resistance. The R_S value for the device is 0.76 Ω. The diameter of semicircle at the high frequency range is due to kinetic resistance to the transfer, known as charge transfer resistance (R_{ct}). The R_{ct} value is 0.79 Ω, result from kinetic transfer of combination of MnO_2 and AC electrode. At the The equivalent distributed resistance (R_d) was obtained from the linear projection of the vertical region of Nyquist plot to the *x*- intercept on the real impedance and subtracting the R_S from the intersection (Kötz & Carlen, 2000). The R_d arises from the ions diffusion resistance into the porous (micropores and mesopores) network of MnO_2//AC supercapacitor device. The calculated R_d value for the device is 0.72 Ω.

The R_S, determined from the high frequency off-set in the real part of complex impedance of the EIS spectrum are contributed by three main factors viz. (i) electrolyte resistance, (ii) electrode resistance and (iii) electrode–electrolyte resistance. The R_S value for the device is 0.76 Ω. The diameter of semicircle at the high frequency range is

due to kinetic resistance to the transfer, known as charge transfer resistance (R_{ct}). The R_{ct} value is 0.79 Ω, result from kinetic transfer of combination of MnO_2 and AC electrode. At the The equivalent distributed resistance (R_d) was obtained from the linear projection of the vertical region of Nyquist plot to the *x*- intercept on the real impedance and subtracting the R_S from the intersection (Kötz & Carlen, 2000). The R_d arises from the ions diffusion resistance into the porous (micropores and mesopores) network of MnO_2//AC supercapacitor device. The calculated R_d value for the device is 0.72 Ω.

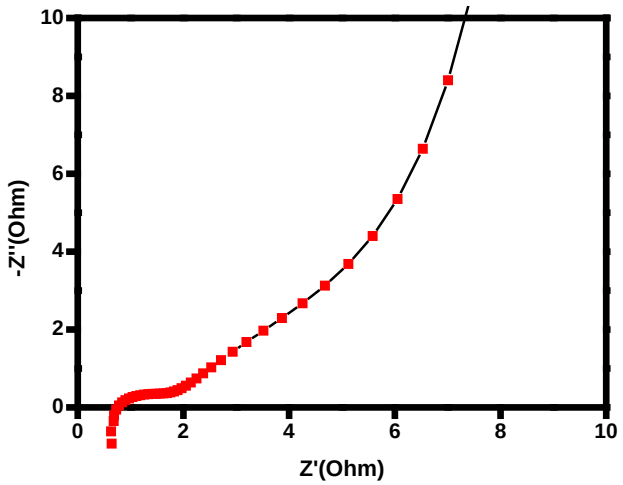

Figure 4. Nyquist plot of MnO_2//AC supercapacitor device.

4.0 CONCLUSION

The synthesis flower shaped MnO_2 and fabricated MnO_2//AC ASC device in aquesous electrolyte were presented. The outcome of the device shows the maximum E_D of 25.79 Wh/kg at P_D 100 W/kg. The stability of the device has been study and shows ~ 95% C_S retention, a promising candidate to build energy storage device using the proposed system.

ACKNOWLEDGEMENT

The authors thank Malaysian Technological University Network (MTUN) Gallery Showcase Research Grant (RDU131201), Postgraduate Research Scheme of UMP (GRS 130317) and Zhejiang Forest Energy Technology Co. Ltd for activated carbon sample.

REFERENCES

Brousse, T., Taberna, P.-L., Crosnier, O., Dugas, R., Guillemet, P., Scudeller, Y., Simon, P. (2007). Long-term cycling behavior of asymmetric activated carbon/MnO_2 aqueous electrochemical supercapacitor. *Journal of Power Sources*. 173(1), 633–641.

Conway, B. E. (1999). *Electrochemical Supercapacitors: Scientific Fundamentals and Technological Applications*. New York: Kluwer Academic Press/Plenum Publishers.

Cottineau, T., Toupin, M., Delahaye, T., Brousse, T., & Bélanger, D. (2005). Nanostructured transition metal oxides for aqueous hybrid electrochemical supercapacitors. *Applied Physics A*. 82(4), 599–606.

Dmowski, W., Egami, T., Swider-Lyons, K. E., Love, C. T., & Rolison, D. R. (2002). Local Atomic Structure and Conduction Mechanism of Nanocrystalline Hydrous RuO_2 from X-ray Scattering. *The Journal of Physical Chemistry B*. 106(49), 12677–12683.

Gao, H., Xiao, F., Ching, C. B., & Duan, H. (2012). High-Performance Asymmetric Supercapacitor Based on Graphene Hydrogel and Nanostructured MnO_2. *ACS Applied Materials & Interfaces*. 4(5), 2801–2810.

Ghodbane, O., Pascal, J.L., & Favier, F. (2009). Microstructural Effects on Charge-Storage Properties in MnO_2-Based Electrochemical Supercapacitors. *ACS Applied Materials & Interfaces*. 1(5), 1130–1139.

Khomenko, V., Raymundo-Piñero, E., & Béguin, F. (2006). Optimisation of an asymmetric manganese oxide/activated carbon capacitor working at 2V in aqueous medium. *Journal of Power Sources*. 153(1), 183–190.

Kim, I.H., & Kim, K.B. (2006). Electrochemical Characterization of Hydrous Ruthenium Oxide Thin-Film Electrodes for Electrochemical Capacitor Applications. *Journal of The Electrochemical Society*. 153(2), A383-A389.

Kötz, R., & Carlen, M. (2000). Principles and applications of electrochemical capacitors. *Electrochimica Acta*. 45(15–16), 2483–2498.

Liang, K., Tang, X., & Hu, W. (2012). High-performance three-dimensional nanoporous NiO film as a supercapacitor electrode. *Journal of Materials Chemistry*. 22(22), 11062-11067.

Liu, J., Jiang, J., Cheng, C., Li, H., Zhang, J., Gong, H., & Fan, H. J. (2011). Co_3O_4 Nanowire@MnO_2 Ultrathin Nanosheet Core/Shell Arrays: A New Class of High-Performance Pseudocapacitive Materials. *Advanced Materials*. 23(18), 2076–2081.

Qu, Q., Zhang, P., Wang, B., Chen, Y., Tian, S., Wu, Y., & Holze, R. (2009). Electrochemical Performance of MnO_2 Nanorods in Neutral Aqueous Electrolytes as a Cathode for Asymmetric Supercapacitors. *The Journal of Physical Chemistry C*. 113(31), 14020–14027.

Simon, P., & Gogotsi, Y. (2008). Materials for electrochemical capacitors. *Nature Materials*. 7(11), 845–854.

Tomko, T., Rajagopalan, R., Lanagan, M., & Foley, H. C. (2011). High energy density capacitor using coal tar pitch derived nanoporous carbon/MnO_2 electrodes in aqueous electrolytes. *Journal of Power Sources*. 196(4), 2380–2386.

Toupin, M., Brousse, T., & Bélanger, D. (2002). Influence of Microstucture on the Charge Storage Properties of Chemically Synthesized Manganese Dioxide. *Chem. Mater*. 14(9), 3946–3952.

Truong, T. T., Liu, Y., Ren, Y., Trahey, L., & Sun, Y. (2012). Morphological and Crystalline Evolution of Nanostructured MnO_2 and Its Application in Lithium–Air Batteries. *ACS Nano*. 6(9), 8067–8077.

Vidyadharan, B., Aziz, R. A., Misnon, I. I., Anil Kumar, G. M., Ismail, J., Yusoff, M. M., & Jose, R. (2014). High energy and power density asymmetric supercapacitors using electrospun cobalt oxide nanowire anode. *Journal of Power Sources*. 270, 526–535.

Wang, Y.-T., Lu, A.-H., Zhang, H.-L., & Li, W.-C. (2011). Synthesis of Nanostructured Mesoporous Manganese Oxides with Three-Dimensional Frameworks and Their Application in Supercapacitors. *The Journal of Physical Chemistry C*. 115(13), 5413–5421.

Yan, J., Wang, Q., Wei, T., & Fan, Z. (2014). Recent Advances in Design and Fabrication of Electrochemical Supercapacitors with High Energy Densities. *Advanced Energy Materials*. 4(4), 1300816.

Yuan, A., & Zhang, Q. (2006). A novel hybrid manganese dioxide/activated carbon supercapacitor using lithium hydroxide electrolyte. *Electrochemistry Communications*. 8(7), 1173–1178.

Zhang, F., Yuan, C., Lu, X., Zhang, L., Che, Q., & Zhang, X. (2012). Facile growth of mesoporous Co3O4 nanowire arrays on Ni foam for high performance electrochemical capacitors. *Journal of Power Sources*. 203, 250–256. doi:10.1016/j.jpowsour.2011.12.001

Zheng, J. P., Cygan, P.J., & Jow, T.R. (1995). Hydrous Ruthenium Oxide as an Electrode Material for Electrochemical Capacitors. *Journal of The Electrochemical Society*. 142(8), 2699-2703.

Zhu, G., Deng, L., Wang, J., Kang, L., & Liu, Z.H. (2013). Hydrothermal preparation and the capacitance of hierarchical MnO_2 nanoflower. *Colloids and Surfaces A: Physicochemical and Engineering Aspects*. 434, 42–48.